CATALYTIC HYDRODEOXYGENATION OF m-CRESOL OVER Ni_2P/HIERARCHICAL ZSM-5

Antonio Berenguer[1], James A. Bennett[2], James Hunns,[2] Inés Moreno[1,3], Juan M. Coronado[1], Adam F. Lee,[2] Patricia Pizarro[1,3], Karen Wilson[2*], David P. Serrano[1,3*]

[1]IMDEA Energy Institute, Avda. Ramón de la Sagra 3, Móstoles, Madrid, Spain.

[2]European Bioenergy Research Institute, Aston University, Aston Triangle, Birmingham, United Kingdom.

[3]Chemical and Environmental Engineering Group, ESCET, Rey Juan Carlos University, c/ Tulipán s/n, Móstoles, Madrid, Spain.

Corresponding authors*:

Tel.: +34 917371120, E-mail address: david.serrano@imdea.org (David P. Serrano). Thermochemical Processes Unit, IMDEA Energy Institute, 28935, Móstoles, Madrid, Spain.

Tel.: +44 (0)121 2044036. E-mail address: k.wilson@aston.ac.uk (Karen Wilson). European Bioenergy Research Institute, Aston University, Birmingham, B4 7ET, UK.

Abstract

Bifunctional catalysts comprising Ni_2P supported over a hierarchical ZSM-5 zeolite (h-ZSM-5) were synthesized and applied to the hydrodeoxygenation (HDO) of m-cresol, a model pyrolysis bio-oil compound. Surface and bulk characterization of Ni_2P/h-ZSM-5 catalysts by XRD, TEM, DRIFTS, TPR, porosimetry and propylamine temperature-programmed desorption reveal that Ni_2P incorporation modifies the zeolite textural properties through pore blockage of the mesopores by phosphide nanoparticles, but has negligible impact of the micropore network. Ni_2P nanoparticles introduce new, strong Lewis acid sites, whose density is proport ional to the Ni_2P loading, accompanied by new Brönsted acid sites attributed to the presence of P-OH moieties. Ni_2P/h-ZSM-5 is ultraselective (> 97 %) for m-cresol HDO to methylcyclohexane, significantly outperforming a reference Ni_2P/SiO_2 catalyst and highlighting the synergy between metal phosphide and solid acid support. m-Cresol conversion was proportional to Ni_2P loading reaching 80 and 91 % for 5 and 10 wt% Ni respectively. Turnover frequencies for m-cresol HDO are a strong function of Ni_2P dispersion, evidencing a structure sensitivity, with optimum activity observed for 4 nm particles.

Keywords: Hydrodeoxygenation; m-cresol; nickel phosphide; hierarchical ZSM-5

1. Introduction

Extensive efforts are being made to develop renewable energy sources to meet growing energy demand and environmental and sociopolitical concerns arising from a current heavy global dependence on fossil fuels. **[1-3]** Lignocellulosic biomass is considered a sustainable and abundant feedstock which can be effectively converted into liquid fuels *via* fast pyrolysis technologies. **[4**4-**5]** Unfortunately, the liquid fraction obtained from biomass fast pyrolysis, known as pyrolysis bio-oil, is unsuitable for direct use as a transportation fuel (or as a fuel additive) because of its low heating value and high corrosiveness caused by the presence of significant oxygenated compounds (ketones, aldehydes, organic acids, furans, phenolic derivatives and lignin-derived oligomers). Such organic compounds are highly reactive, promoting the formation of ethers, acetals, hemiacetals and heavier organics through condensation reactions, resulting in low bio-oil stability. Accordingly, pyrolysis bio-oil requires upgrading to obtain a liquid fuel with properties similar to those derived from fossil resources. **[1,2,6]**

Catalytic hydrodeoxygenation (HDO) is an effective bio-oil upgrading strategy which involves the stabilization and selective removal of oxygen from the raw bio-oil using moderate temperatures and medium-high hydrogen pressures in the presence of heterogeneous catalysts. Hydrodeoxygenation normally occurs *via* hydrogenolysis of C-O bonds with the consequent elimination of oxygen as water. Decarboxylation/decarbonylation, hydrogenation-hydrocracking of large molecules, and hydrogenation reactions of unsaturated molecules, can also occur during HDO. **[7-9]**

Due to the complex composition of pyrolysis bio-oils, and the difficulty of deconvoluting the resultant possible reactions during bio-oil HDO, catalyst development studies typically employ model compounds to obtain fundamental mechanistic insight into bio-oil upgrading. **[10]** Lignin derived phenolic compounds (phenols, guaiacols, syringols, etc.) are one of the most abundant families in pyrolysis bio-oils, and extensively contribute to bio-oil instability and aging, being the main source of coke deposition over catalyst surfaces. Hydrogenation, deoxygenation and ring-opening of phenolic derivatives thus represent critical challenges to commercial bio-oil upgrading. **[9-13]**

HDO catalysts are usually classified in two categories: conventional hydrotreating catalysts, such as sulfided CoMo and NiMo/γ-Al_2O_3, and unconventional catalysts including supported noble and transition metals. **[14-16]** Noble metal catalysts, such as Pd, Ru, Pt and Rh deposited on active carbon, Al_2O_3 and ZrO_2,

have been extensively used for HDO of phenolic model compounds to yield aromatic hydrocarbons and saturated cyclic compounds. Compared to conventional sulfided catalysts, noble metal catalysts are more active and do not require the addition of sulfur containing compounds to prevent catalyst deactivation. Nevertheless, the high cost of such noble metals limits their industrial application. **[17-20]** Alternative transition metals, notably Ni and Ni/Cu alloys, have been also explored for HDO of model compounds and raw bio-oils **[1,** 21-23**].** However, Ni catalysts promote secondary reactions such as C-C bond hydrogenolysis, methanation and decarbonylation, resulting in carbon loss and a high hydrogen consumption. In contrast, transition metal phosphides appear promising catalysts for pyrolysis bio-oil HDO for various phenolics including phenol, guaiacol, p-cresol and anisole **[24-**29**]**: Ni_2P exhibits superior HDO performance to Co_2P, Fe_2P, WP and MoP. This enhanced performance is attributed to the higher d-electron density of Ni_2P phase, and a combination of structural and electronic influences of phosphorus atoms on the transition metal sites, which favors oxygenate adsorption and C-O bond cleavage. **[24, 27-**29**]** According to the literature, the formation of the Ni_2P phase requires a high temperature during the reduction treatment and is favored by the presence of phosphorus excess during the support impregnation. In this sense, several studies established that optimal molar Ni/P ratio is ranged between 1-1.4. Higher ratios promote the formation of less active nickel phosphide phases ($Ni_{12}P_5$ and Ni_3P) while lower ratios yield to higher Ni_2P particle size, leading to a lower catalytic activity as a consequence of the reduced number of available centers for hydrogenation. **[30-33]**

Ni_2P is often supported over neutral solids including SiO_2, SBA-15, MCM-41 or carbons. **[29, 34-**36**]** However, recent investigations have demonstrated acidic supports can enhance the deoxygenation efficiency of metal catalysts. The resulting bifunctional catalysts combine a metal component which activates C=C and C=O bonds towards hydrogenation, while acid sites promotes dehydration, hydrocracking and isomerization, favoring the complete deoxygenation of refractory phenolic derivatives. [7,26,**31**] Zeolites are of especial interest as the acid component of HDO bifunctional systems due to their tunable acidity and stability under severe reaction conditions. Zeolites including ZSM-5, Beta, MCM-22 and Y have been recently employed as supports for noble and transition metal active phases **[10,21,38-40]**, however there are no systematic studies on their promotion by metal phosphides for HDO.

Hierarchical zeolites are a novel class of materials possessing secondary mesopores of 2-50 nm diameter in addition to the intrinsic zeolitic micropore framework. This bimodal pore architecture may be advantageous

when employing hierarchical zeolites as supports for catalytically active metal nanoparticles, wherein mesopores may enhance the active phase dispersion. Such hierarchical materials also present less diffusional and steric constraints than conventional microporous zeolites, which is especially important for the transformation of large bio-molecules. Hierarchical ZSM-5 and Y zeolites functionalized with Pt and Ni are promising bifunctional catalysts. **[41-43]**

Here we investigate possible synergies between metallic Ni_2P nanoparticles and a hierarchical ZSM-5 zeolite for m-cresol HDO (as a model for the most abundant and refractory compounds in pyrolysis bio-oils) as a function of phosphide loading. Physicochemical and catalytic properties of these materials were determined and their performance compared with those of Ni_2P over a non-acidic SiO_2 support.

2. Experimental

2.1. Materials preparation

2.1.1. Synthesis of h-ZSM-5

Hierarchical ZSM-5 (h-ZSM-5) was prepared following a literature procedure based on the crystallization of silanized protozeolitic units. **[44]** Typically, a clear gel with a molar composition of 1 Al_2O_3: 80 SiO_2: 14.4 TPAOH: 2015 H_2O was prepared from tetraethoxysilane (TEOS, 98 wt%, Aldrich) and aluminium isopropoxide (AIP, 98 wt%, Aldrich) as silica and aluminum precursors and tetrapropylammonium hydroxide (TPAOH, 40 wt%, Alfa) as template. This solution was pre-crystallized under reflux and stirring at 90 ºC for 20 h. Subsequently, the resulting zeolitic seeds were functionalized by reaction with a silanization agent, phenylaminopropyltrimethoxysilane (PHAPTMS, 95 wt%, Aldrich), at 90 ºC for 6 h. The organosilane was added in a proportion of 8 mol % relative to the initial silica content of the gel. Finally, the resulting solution was crystallized in a Teflon-lined stainless-steel autoclave at 170 ºC for 7 days. The solid product obtained was separated by centrifugation, washed several times with distilled water, dried overnight at 110 ºC and calcined at 550 ºC for 5 h under static air.

2.1.3. Metal phosphide incorporation

Supported nickel phosphide catalysts were prepared by a temperature-programmed reduction (TPR) method. **[45]** The zeolite was first impregnated with an aqueous solution of nickel and phosphorus precursors,

$(NH_4)_2HPO_4$ (Aldrich) and $Ni(NO_3)_2 \cdot 6H_2O$ (Aldrich) using an equimolar Ni:P ratio, and nominal nickel loadings of 2.5, 5 and 10 wt%. The supported materials were dried overnight at room temperature and subsequently at 120 ºC for 24 h. Dried samples were then calcined at 500 ºC for 4 h. Resulting phosphate catalysts were pelletized, crushed and sieved to 40-60 mesh (250-180 μm), prior to reduction under flowing H_2 (80 ml/min) in a tubular furnace: samples were heated from room temperature to 350 ºC at 5 ºC/min; from 350 ºC to 650 ºC at 1 ºC/min and then held isothermally for 3 h. Immediately after the last reduction step samples were passivated by the progressive introduction of synthetic air during cooling to room temperature. Passivation was used to create an oxide layer to inhibit deeper sample oxidation on air exposure during transfer to the catalytic reactor. Ni_2P supported on a commercial SiO_2 sample (Aldrich, fumed powder, 0.2-0.3 μm average particle size, surface area 200 $m^2/g \pm 25$ m^2/g) was similarly prepared using with a nominal 10 wt% nickel loading.

2.2. Catalyst characterization

X-ray diffraction (XRD) patterns of catalysts were recorded with a Philips PW 3040/00 X'Pert MPD/MRD diffractometer using Cu K_α radiation operated at 45 kV and 40 mA. Crystalline phases were indexed through comparison with the JCPDS (Joint Committee on Powder Diffraction Standards) database.

Argon adsorption-desorption isotherms were measured at 87 K using a Quantrachrome Autosorb-1 analyzer, following degassing at 573 K for 5 h prior to analysis. Total surface areas were calculated according to the BET method, while pore size distributions, and surface areas and pore volume associated with the micro- and mesopore networks calculated using the NL-DFT model assuming cylindrical pore geometry.

Transmission electron microscopy (TEM) images were recorded in a PHILIPS TECHNAI 20 electron microscope operating at 200 kV and 2.7 Å resolutions. Samples were dispersed in acetone and dropped on a carbon-coated copper grid. Nickel, aluminum and phosphorus contents were determined on a Varian VISTA-MPX Inductively Coupled Plasma-Optical Emission Spectrometer (ICP-OES).

Acid strength was determined by propylamine thermogravimetric analysis coupled with mass spectrometry (TGA-MS). Prior to analyses, samples were wet-impregnated with propylamine and then dried overnight under vacuum at 60 °C. Thermal desorption was performed on a Mettler Toledo TGA/DSC 2 StarSystem between 40 and 800 °C under a He flow of 20 mL/min, using a ramp rate of 10 °C/min and gas

detection through a Pfeiffer Vacuum, ThermoStar MS. Chemisorbed propylamine decomposes into propene and ammonia over acid sites.

Brönsted/Lewis acid character was studied by means of Diffuse Reflectance Infrared Fourier Transform Spectroscopy (DRIFTS) using pyridine as probe molecule. Ex situ pyridine adsorption was performed by saturation of diluted samples (5 wt% in KBr). Excess physisorbed pyridine was removed under vacuum at 60 °C prior to spectral acquisition on a Nicolet Avatar spectrometer at 50 °C in a Harrick environmental cell.

Metal dispersion was determined by temperature programmed desorption of H_2 (H_2-TPD) employing a Micromeritics AUTOCHEM 2910 apparatus on 100 mg of sample loaded in a quartz U-tube reactor. Sample were reduced at 650 °C under flowing 10 vol% H_2 in Ar (with a stream of 50 ml/min) for 30 min., then cooled to 60 °C and held for 60 min. Subsequently, the H_2/Ar mixture was changed to 50 ml/min of Ar and held for 30 min. Chemisorbed hydrogen was measured from its subsequent desorption on heating from 60 to 600 °C at 10 °C/min. Nickel dispersions (% D) were calculated from the volume of chemisorbed H_2 [46] assuming atomic hydrogen only binds to nickel surface atoms with a H:Ni stoichiometry of 1.

2.3. Catalytic experiments

The HDO catalytic activity of the metal phosphide supported materials was evaluated in a 50 mL stainless steel Parr autoclave using m-cresol as model compound. Initially, 50 ml of a solution containing 1.5 wt% of m-cresol (98 wt%, Aldrich) in dodecane (99 wt%, Aldrich), together with 100 mg of catalyst, were loaded into the reactor. Prior to the HDO catalytic tests the sealed autoclave was purged by flowing pure N_2 at room temperature. The reactor was then heated to the reaction temperature (200 ºC) under vigorous stirring (800 rpm) and once at temperature pressurized with 25 bar pure H_2. Reactant and liquid products were analyzed off-line by gas chromatography (Varian 3800 GC) equipped with a FID detector and VF-5ms column (30 m x 0.25 mm x 0.25 μm).

Catalytic performance was evaluated by several parameters: m-cresol conversion (X_{CRE}), selectivity towards *i* product (S_i), deoxygenation degree (HDO), dearomatization degree (HDA) and TOF (Turnover Frequency) according to the following equations:

$$(1) \qquad X_{CRE}\,(\%) = \frac{n^0_{CRE} - n^F_{CRE}}{n^0_{CRE}} \times 100$$

(2) $$S_i = \frac{n_i}{n^0_{CRE} - n^F_{CRE}} \times 100$$

(3) $$\text{HDO (\%)} = \left(1 - \frac{\sum_i n_i O_i}{n^0_{CRE} \times X_{CRE}}\right) \times 100$$

(4) $$\text{HDA (\%)} = \left(1 - \frac{\sum_i n_i A_i}{n^0_{CRE} \times X_{CRE}}\right) \times 100$$

(5) $$\text{TOF (min}^{-1}\text{)} = \frac{V_{CRE}}{W \times M}$$

Where n^0_{CRE} and n^F_{CRE} represent the initial and final moles of m-cresol, respectively; n_i the moles of product i; O_i the number of oxygen atoms in product I; A_i the number of aromatic rings in product *i*; V_{CRE} the rate of conversion of m-cresol; W the mass (g) of active phase; and M the molecular weight ($mmol \cdot g^{-1}$) of active phase.

3. Results and discussion

3.1. Catalyst characterization

Catalyst were reduced at 650 °C and subsequently passivated under air in order to preserve a metal phosphide phase during under atmospheric exposure. **Fig. 1** shows powder XRD patterns of Ni_2P/h-ZSM-5 samples and the parent zeolite. All materials exhibited high crystallinity characteristic of the parent MFI zeolite structure, with the intensity and position of the MFI reflections (and hence zeolite crystallinity) unaffected by the reduction pretreatment. Additional peaks at 2θ = 40.7, 44.6 and 47.4 ° were assigned to (111), (201) and (210) reflections of Ni_2P (PDF code: 03-065-1989), whose formation was promoted by the excess of P used during the support impregnation ($[Me/P]_{MOL}$ ~1.0) and the high reduction temperature during synthesis. **[30-33]** No additional peaks due to metallic Ni or ordered phosphate phases were observed, consistent with the complete reduction of nickel and phosphorus precursors. Ni_2P reflections broadened and weakened with decreasing Ni loading, being almost undetectable for the 2.5Ni_2P/h-ZSM-5 sample, indicating a decrease in nickel phosphide nanoparticle size, in agreement with particle size distributions visualized by TEM (**Fig. 2**). TEM images of 10Ni_2P/h-ZSM-5 reveal a broad distribution of phosphide nanoparticles with a mean particle size of 15 nm (although some >50 nm particles were also present). Ni_2P nanoparticles were more

homogeneously dispersed over the zeolite for the $5Ni_2P$/h-ZSM-5 sample, which exhibited a smaller mean particle size around 7 nm, and the $2.5Ni_2P$/h-ZSM-5 sample for which the mean particle size was ~4 nm.

Fig. 3 shows Ar adsorption-desorption isotherms and corresponding pore size distributions for the supported phosphides and parent zeolite (subjected to an identical reductive and passivation pretreatment). All samples exhibited an intermediate shape between type I and IV isotherms (according to the IUPAC classification) due to the co-existence of micro- and mesopores: the strong adsorption observed at low relative pressures (P/P_0 <0.2) is characteristic of microporous materials, while the continuous Ar uptake at intermediate relative pressures is typical of mesoporous solids. The presence of a bimodal pore structure was confirmed from NL-DFT calculations which reveal a narrow and well-defined peak at 5 Å, attributed to the zeolitic micropores of the MFI crystalline structure, in addition to a broad pore distribution spanning 20-60 Å arising from the mesopore network.

For all Ni loadings, a small decrease in Ar adsorption was observed following metal phosphide deposition, although a common isotherm shape was observed. Consequently, the textural properties of the parent support (Table 1) exhibited only small variations upon nickel phosphide incorporation, with the total and mesopore surface areas and volumes around 45 % lower than the parent zeolite, whereas the corresponding micropore areas and volumes showed minimal change. These results indicate that nickel phosphide nanoparticles were largely confined to the mesopores. Phosphide particle sizes for the $2.5Ni_2P$/h-ZSM-5 sample of 4 nm lie within the range of the zeolite mesopore diameters (2-6 nm), and hence it is reasonable to assume that most of these nanoparticles are located within the mesopores. In contrast, TEM shows that the larger phosphide nanoparticles formed for higher Ni loadings (>7 nm) are unlikely to reside within the mesopores, and a significant proportion are expected to distribute over the outer surface of the zeolite, and hence not block mesopores.

The chemical composition of both catalysts and raw support were determined by ICP-OES analyses (**Table 1**). In all cases the actual Ni:P molar ratios were between 1.00 and 1.19, close to the nominal ratio employed during impregnation. XRD indicates that despite the equimolar ratio of Ni and P precursors, only a crystalline metal-rich Ni_2P phase formed during thermal processing, and we propose that this residual phosphorus is be present as a highly dispersed (molecular) phosphite or phosphate species.

Fig. 4 shows DRIFT spectra of the Ni_2P/h-ZSM-5 and parent zeolite following pyridine chemisorption. Absorption features at 1447, 1547, 1490 and 1638 cm^{-1} observed for the parent zeolite are assigned to pyridine adsorbed at Lewis acid sites (PyL, 1447 cm^{-1}) arising from partially coordinated Al atoms and extra-framework aluminum in the form of AlO^+, $Al(OH)^{2+,}$ $Al(OH)_3$, $Al(OH)_2^+$ species. The 1490 cm^{-1} band is attributed to pyridine molecules adsorbed over Brönsted and Lewis acid sites, while that at 1596 cm^{-1} corresponds to pyridine hydrogen-bonded to weak free silanol groups. **[**47**]** The intensity of the latter band progressively decreased with Ni loading, presumably due to surface and pore blocking by the metal phosphide nanoparticles. Ni_2P/h-ZSM-5 samples also exhibited a new absorption band appeared at 1608 cm^{-1} whose intensity increased with Ni loading, and is attributed to the genesis of new Lewis acid sites arising from Ni→P electron transfer and the formation of $Ni^{\delta+}$ species. The blue shift of this new Lewis acid band relative to the parent h-ZSM-5 (1447 cm^{-1} and 1596 cm^{-1}) indicates that the former possesses stronger acidity. **[49, 49]** Bands at 1547 and 1638 cm^{-1} are commonly attributed to pyridinium ions (PyH^+) coordinated to Brönsted acid sites; these are broadened and red shifted in the Ni_2P/h-ZSM-5 samples, suggesting weaker Brönsted acidity following nickel phosphide deposition, which may again reflect blocking of Brönsted sites in the parent zeolites. However, suppression of the intrinsic Brönsted acidity of the zeolite may be partially compensated by the presence of molecular P-OH species as noted above.

Acid properties were quantified by TGA-MS after following propylamine chemisorption. The latter is a weak base that reacts with accessible acid sites to evolve propene and ammonia during thermal processing; the desorption temperature of reactively-formed propene is inversely proportional to acid strength. **Fig. 5** displays propene desorption profiles from propylamine TGA-MS for Ni_2P/h-ZSM-5 and the parent h-ZSM-5 zeolite, alongside that of a Ni_2P/SiO_2 reference material. The parent zeolite exhibited two propene desorptions centered at 412 and 475 ºC, with the former assigned to the Lewis acid sites and the latter to acidic bridging Si–OH–Al groups (typical Brönsted acid sites in the zeolite). **[50, 51]** The higher intensity of the 412 ºC desorption for the h-ZSM-5 evidences dominant Lewis acidity associated with the secondary porosity. **[**47**]** The Ni_2P/SiO_2 sample exhibited only a broad desorption around 375 ºC, which, owing to the lack of acidity of the SiO_2 support, can be only assigned to Lewis acid sites generated by Ni_2P species. A weak higher temperature shoulder also hints at the existence of a small proportion of weaker acid sites, probably related to P-OH groups. The total acid

site loading of the silica sample was three times lower than that of the parent zeolitic (0.34 versus 0.95 mmol/g, respectively). Propene desorption spectra for Ni_2P/h-ZSM-5 materials were intermediate between those of the parent zeolite and Ni_2P/SiO_2, exhibiting desorption peaks at 370 ºC and 454 ºC. The first was coincident with that observed from Ni_2P/SiO_2, and is therefore attributed to Lewis acid sites arising from Ni_2P nanoparticles; the second is attributed to Brönsted acid sites from the parent h-ZSM-5 and surface P-OH groups. The total acid site loadings of all Ni_2P/h-ZSM-5 materials were similar to the parent zeolite, indicating that phosphide suppression of the zeolite acidity was quantitatively compensated by the formation of new Lewis and Brönsted sites.

3.2. m-Cresol catalytic activity

Catalytic HDO of m-cresol was explored over the Ni_2P/h-ZSM-5 bifunctional catalysts in a batch reactor at 200 ºC under 25 bar of H_2. m-Cresol hydrodeoxygenation is proposed to occur through two competing reaction pathways (**Fig. 6**). The first involves direct hydrogenation of the aromatic ring (HYD) leading to 3-methylcyclohexanol, which can be sequentially dehydrated and hydrogenated to obtain the fully deoxygenated methylcyclohexane product. The second pathway follows direct C-O bond scission of m-cresol (DDO route) yielding toluene as intermediate product, which is subsequently hydrogenated to methylcyclohexane. **[**41**,** 52**]**

Fig. 7 shows reaction profiles for m-cresol conversion and product formation (selectivity) as a function of Ni loading over the Ni_2P/h-ZSM-5 and $10Ni_2P/SiO_2$ reference. In order to evaluate the possible effect of the catalyst acidity on the solvent stability, a blank experiment without m-Cresol was performed using the same reaction conditions, revealing a negligible dodecane hydrocracking. $10Ni_2P/SiO_2$ reference exhibited inferior m-cresol conversion compared to the equivalent loading $10Ni_2P$/h-ZSM-5 (only 50 % versus 91 %), highlighting the importance of an acidic support. For the Ni_2P/h-ZSM-5 materials, m-Cresol conversion was proportional to Ni loading, and in all cases m-cresol conversion increased almost linearly with reaction time suggesting minimal catalyst deactivation under our reaction conditions. Corresponding TOFs (normalized per Ni_2P) are shown in **Fig. 8**, together with the Ni dispersion, and evidence a direct correlation between the Ni (Ni_2P) particle size and activity, indicating HDO is structure sensitive being favored over small (<7 nm) phosphide particles. The $10Ni_2P/SiO_2$ and Ni_2P/h-ZSM-5 catalysts also exhibited significant differences in product selectivity (**Fig. 7**).

In the initial stage of reaction, $10Ni_2P/SiO_2$ only produces 3-methylcyclohexanol, whose yield subsequently decreases to reach a final selectivity of 60 % after 6 h reaction as a consequence of secondary methylcyclohexane formation. In contrast, Ni_2P/h-ZSM-5 exhibit far more rapid conversion of intermediate methylcyclohexanol, such that the final methylcyclohexane selectivity approaches 100 % after 6 h independent of Ni loading. The zeolite support is thus critical for complete m-cresol deoxygenation. For the h-ZSM-5 support Ni_2P catalysts, the rate of methylcyclohexanol removal was also inversely proportional to Ni loading, suggesting that the Brönsted acidity of P-OH groups may also play an important role in methylcyclohexanol dehydration to methylcyclohexane. Since only trace toluene was observed, m-cresol HDO reaction preferentially proceeds through aromatic ring hydrogenation (HYD route) over all Ni_2P catalysts. Comparison of the product evolution over Ni_2P/SiO_2 and Ni_2P/h-ZSM-5 catalysts suggest that the first HYD step (m-cresol conversion to 3-methylcyclohexanol) is catalyzed by Ni_2P active sites alone, while C-O bond scission and dehydration are promoted by the zeolite acidity.

Overall m-cresol conversion and HDO and HDA efficiencies are compared in **Fig. 9**. All the Ni_2P supported catalysts exhibited high HDA efficiencies, independent of the support, as expected if m-cresol HDO preferentially occurs via the direct hydrogenation route which involves the saturation of aromatic rings catalyzed by the metallic Ni_2P phase. The HDO degree exhibited by Ni_2P/SiO_2 was relatively low (~39 %) compared to the efficiencies of the Ni_2P/h-ZSM-5 materials which were all around 100 %, again highlighting the synergy between metal nanoparticle and solid acid support components necessary for hydrodeoxygenation.

Finally, the material $5Ni_2P$/h-ZSM-5 was reutilized in second reaction cycle. In this experiment, the m-Cresol conversion attained over the spent catalyst was 98 % of the conversion obtained using the fresh material, which denotes the high stability of this catalyst. However, minor changes were detected in terms of product distribution obtained. As it can be appreciated in **Fig. 10**, the selectivity towards the fully deoxygenated product (methylcyclohexane) is a 10 % lower over the spent catalyst, increasing the selectivity towards methylcyclohexanol. This fact suggests a small lost in the overall HDO activity of this material from the first to the second reaction, probably due to the formation of carbonaceous residues.

4. Conclusions

Ni_2P/h-ZSM-5 catalysts having Ni loadings spanning 2.5-10 wt% were synthesis and tested for the hydrodeoxygenation (HDO) of m-cresol. Metal phosphide incorporation has little impact on the crystallinity or microporosity of the hierarchical ZSM-5 zeolite, but modifies both the Lewis and Brönsted acid character of the support, and introduces new strong Lewis acid sites and small amounts of new Brönsted sites possibly arising from P-OH moieties. The Ni_2P dispersion is inversely proportional to Ni loading, with 2.5 wt% Ni favoring uniform 4 nm particles distributed throughout the mesopore network. Activity for m-cresol HDO is proportional to Ni_2P content, but exhibits structure sensitivity with small particles offering higher TOFs. Ni_2P/h-ZSM-5 are ultraselective for the complete hydrodeoxygenation of m-cresol to methylcyclohexane, with reaction proceeding through a direct hydrogenation pathway and methylcyclohexanol intermediate. Brönsted acidity from the zeolite support (and possible P-OH functions) is critical for methylcyclohexanol dehydration, highlighting the importance of bifunctional catalysts possessing both acid and metal active sites for m-cresol HDO.

5. Acknowledgements

We thank the Spanish Ministry of Economy and Competitiveness through CATPLASBIO (CTQ2014-60209-R) and the regional government of Madrid through RESTOENE-2 (Ref: S2013/MAE-2882), Consejería de Educación de la Comunidad de Madrid), and the EPSRC for financial support (EP/K036548/2 and EP/N009924/1).

6. References

1. M. Patel, A. Kumar, Renew. Sustain. Energy Rev. 58 (2016) 1293-1307.

2. P.M. Mortensen, J.D. Grunwaldt, P.A. Jensen, K.G. Knudsen, A.D. Jensen, Appl. Catal. A: Gen. 407 (2011) 1-19.

3. A.V. Bridgwater, D. Meier, D. Radlein, Org. Geochemistry 30 (1999) 1479-1493.

4. G.W. Huber, S. Iborra, A. Corma, Chem. Rev. 106 (2006) 4044-4098.

5. S. Xiu, A. Shahbazi, Renew. Sustain. Energy Rev. 16 (2012) 4406-4414.

6. K. Jacobson, K.C. Maheria, A.K. Dalai, Renew. Sustain. Energy Rev. 23 (2013) 91-106.

7. A.M. Robinson, J.E. Hensley, J.W. Medlin, ACS Catal. 6 (2016) 5026-5043.

8. X. Li, G. Chen, C. Liu, W. Ma, B. Yan, J. Zhang, Renew. Sustain. Energy Rev. 71 (2017) 296-308.

9. Q. Bu, H. Lei, A.H. Zacher, L. Wang, S. Ren, J. Liang, Y. Wei, Y. Liu, J. Tang, Q. Zhang, R. Ruan, Bioresource Technol. 124 (2012) 470-477.

10. H. Shafaghat, P. S. Rezaei, W. M. A. W. Daud, J. Ind. Eng. Chem 35 (2016) 268-276.

11. C.J. Chen, W. S. Lee, A. Bhan, Appl. Catal. A: Gen. 510 (2016) 42-48.

12. I. Graça, A.M. Carmo, J.M. Lopes, M.F. Ribeiro, Fuel 140 (2015) 484-494.

13. D.A. Ruddy, J.A. Schaidle, J.R. Ferrell, J. Wang, L. Moens, and J.E. Hensley, Green Chem. 16 (2014) 454-490.

14. V.N. Bui, G. Toussaint, D. Laurenti, C. Mirodatos, C. Geantet, Catal. Today 143 (2009) 172-178.

15. A.L. Jongerius, R. Jastrzebski, P.C.A. Bruijnincx, B.M. Weckhuysen, J. Catal. 285 (2012) 315-323.

16. O.I. Senol, T.R. Viljava, A.O.I. Krause, Catal. Today 100 (2005) 331-335.

17. Y. Bie, J. Lehtonen, J. Kanervo, Appl. Catal. A: Gen. 526 (2016) 183-190.

18. J. Wildschut, M. Iqbal, F.H. Mahfud, I. Melian-Cabrera, R.H. Venderbosch, H.J. Heeres, Energy Environ. Sci. 3 (2010) 962-970.

19. S. Oha, H. Hwang, H.S. Choi, J.W. Choi, Fuel 153 (2015) 535-543.

20. A.J. Foster, P.T.M. Do, R. F. Lobo, Top. Catal. 55 (2012) 118-128.

21. X. Zhang, T. Wang, L. Ma, Q. Zhang, T. Jiang, Bioresource Technol. 127 (2013) 306-311.

22. S. Sitthisa, D. Resasco, Catal. Lett. 141 (2011) 784-791.

23. S.A. Khromova, A.A. Smirnov, O.A. Bulavchenko, A.A. Saraev, V.V. Kaichev, S.I. Reshetnikov, V.A. Yakovlev, Kinet. Catal. 55 (2014) 69-78.

24. V.O.O. Goncalves, P. M. de Souza, V. T. da Silva, F. B. Noronh, F. Richard, Appl. Catal. B: Environ. 205 (2017) 357-367.

25. S. T. Oyama, J. Catal. 216 (2016) 343-352.

26. A. Berenguer, T.M. Sankaranarayanan, G. Gómez, I. Moreno, J.M. Coronado, P. Pizarro, D.P. Serrano, Green Chem. 18 (2016) 1938-1951.

27. H.Y. Zhao, D. Li, P. Bui, S.T. Oyama, Appl. Catal. A: Gen. 391 (2011) 305-310.

28. K. Li, R. Wang, J. Chen, Energ. Fuels 25 (2011) 854-863.

29. J.S. Moon, E. G. Kim, Y.K. Lee, J. Catal. 311 (2014) 144-152.

30. S.T. Oyama, X.Wang, Y.K. Lee, K. Bando, F.G. Requejo, Journal of Catalysis 210 (2002) 207–217.

31. Y. Yang, C. Ochoa-Hernández, P. Pizarro, V.A. de la Peña O'Shea, J.M. Coronado, D.P. Serrano, Fuel 144 (2015) 60-70.

32. J. A. Cecilia, A. Infantes-Molina, E. Rodríguez-Castellón, A. Jiménez-López, Journal of Catalysis, 263 (2009) 4-15.

33. J. Chen, M. Han, S. Zhao, Z. Pan, Z. Zhang, Catal. Sci. Technol. 6 (2016) 3938-3949.

34. T.I. Korányi, Z. Vít, J.B. Nagy, Catal. Today. 130 (2008) 80-85.

35. N. Koike, S. Hosokai, A. Takagaki, S. Nishimura, R. Kikuchi, K.I. Ebitani, Y. Suzuki, S.T. Oyama, J. Catal. 333 (2016) 115-126.

36. Y. Yang, J. Chen, H. Shi, Energ. Fuels 27 (2013) 3400-3409.

37. T. Cordero-Lanzac, R. Palos, J. M. Arandes, P. Castaño, J. Rodríguez-Mirasol, T. Cordero, J. Bilbao, Appl. Catal. B: Environ. 203 (2017) 389-399.

38. Y. Li, C. Zhang, Y. Liu, S. Tang, G. Chen, R. Zhang, X. Tang, Fuel 189 (2017) 23-31.

39. F. Anaya, L. Zhang, Q. Tan, D. E. Resasco, J. Catal. 328 (2015) 173-185.

40. J.S. Yoon, T. Lee, J.W. Choi, D.J. Suh, K. Lee, J.M. Ha, J.Choi, Catal. Today (2017) In Press. (http://doi.org/10.1016/j.cattod.2016.10.033)

41. J.A. Hunns, M. Arroyo, A.F. Lee, J.M. Escola, D. Serrano, K. Wilson, Catal. Sci. Technol. 6 (2016) 2560-2564.

42. H.W. Lee, B.R. Jun, H. Kim, D.H. Kim, J.K. Jeon, S.H. Park, C.H. Ko, T.W. Kim, Y.K. Park, Energy 81 (2015) 33-40.

43. T. M. Sankaranarayanan, A. Berenguer, C. Ochoa-Hernández, I. Moreno, P. Jana, J. M. Coronado, D. P. Serrano and P. Pizarro, Catal. Today 243 (2015) 163-172.

44. D.P. Serrano, J. Aguado, J.M. Escola, J.M. Rodríguez, Á. Peral, Chem. Mater. 18 (2006) 2462-2464.

45. R. Prins, M. E. Bussell, Catal. Letters. 142 (2012) 1413-1436.

46. R. Wojcieszak, S. Monteverdi, M. Mercy, I. Nowak, M. Ziolek, M.M. Bettahar, Appl. Catal. A: Gen. 268 (2004) 241-253.

47. D.P. Serrano, R.A. García, G. Vicente, M. Linares, D. Procházková, J. Cejka, J. Catal. 279 (2011) 366-380.48. S.T. Oyama, X. Wang, F. Requejo, T. Sato, Y. Yoshimura, J. Catal.209 (2002) 1-5.

49. D. Li, P. Bui, H.Y. Zhao, S.T. Oyama, T. Dou, Z.H. Shen, J. Catal. 290 (2012)1-12.

50. R.J. Gorte, Catal. Letters. 62 (1999) 1-13.

51. L.M. Parker, D.M. Bibby, R.H. Meinhold, Zeolites 5 (1985) 384-388.

52. P.T.M. Do, A.J. Foster, J. Chen, R.F. Lobo, Green Chem. 14 (2012) 1388-1397.

Table 1. Physicochemical properties of the Ni_2P/h-ZSM-5 samples and the raw support.

Sample	S_{BET} [a] ($m^2 g^{-1}$)	$S_{MES+EXT}$ [b] ($m^2 g^{-1}$)	S_{MIC} [b] ($m^2 g^{-1}$)	V_{MIC} [b] ($cm^3 g^{-1}$)	$V_{MES+EXT}$ [b] ($cm^3 g^{-1}$)	Ni (%wt)	$[Ni/P]_{MOL}$ [c]
h-ZSM-5 (650 ºC reduced)	500	226	275	0.163	0.306	---	---
2.5Ni_2P/h-ZSM-5	407	145	262	0.156	0.228	2.89	1.00
5Ni_2P/h-ZSM-5	407	146	261	0.156	0.250	6.07	1.10
10Ni_2P/h-ZSM-5	390	132	259	0.154	0.246	11.13	1.19

[a] BET surface area from Ar adsorption-desorption isotherms (87 K).
[b] Calculated by applying the NL-DFT model to Ar adsorption-desorption isotherms (87 K).
[c] Estimated from ICP-AOS analyses.

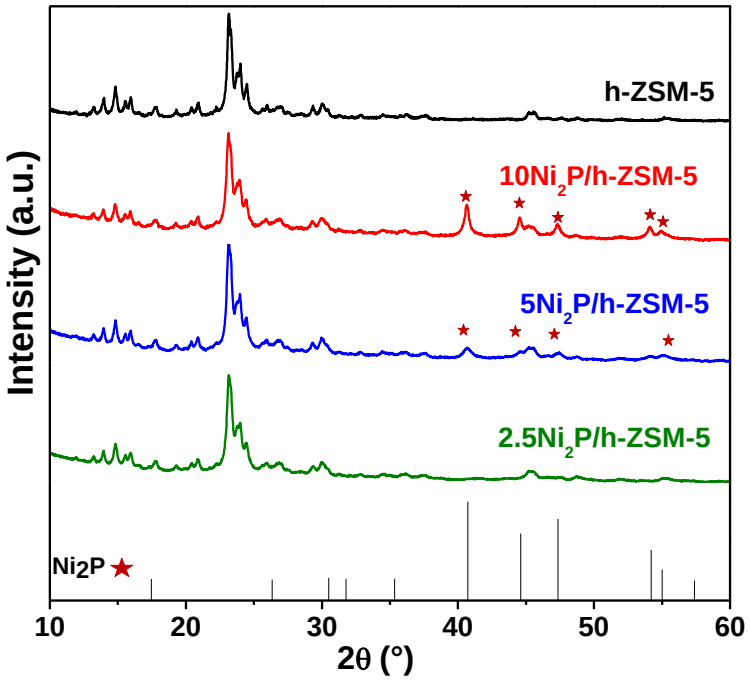

Fig. 1. Wide angle X-ray diffraction patterns of Ni_2P/h-ZSM-5 and parent support.

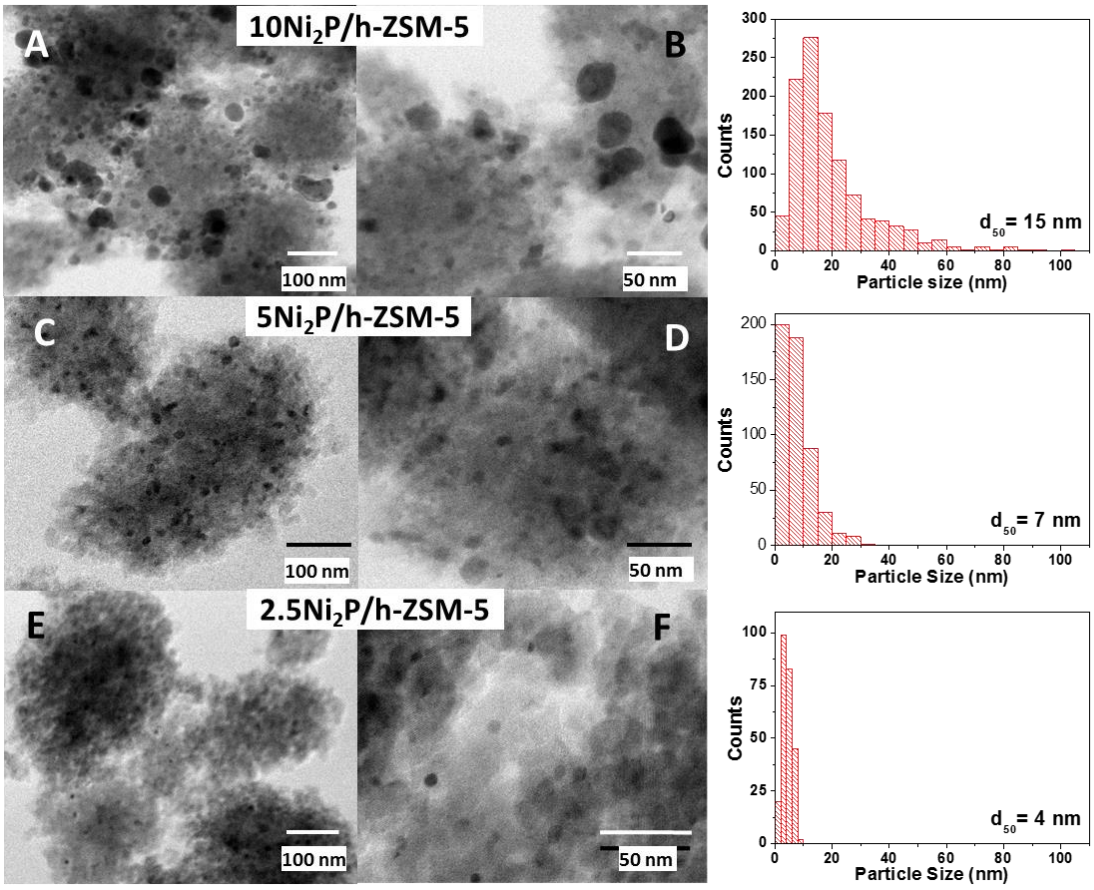

Fig. 2. (A-F) TEM micrographs of Ni_2P/h-ZSM-5 and corresponding Ni_2P particle size distributions.

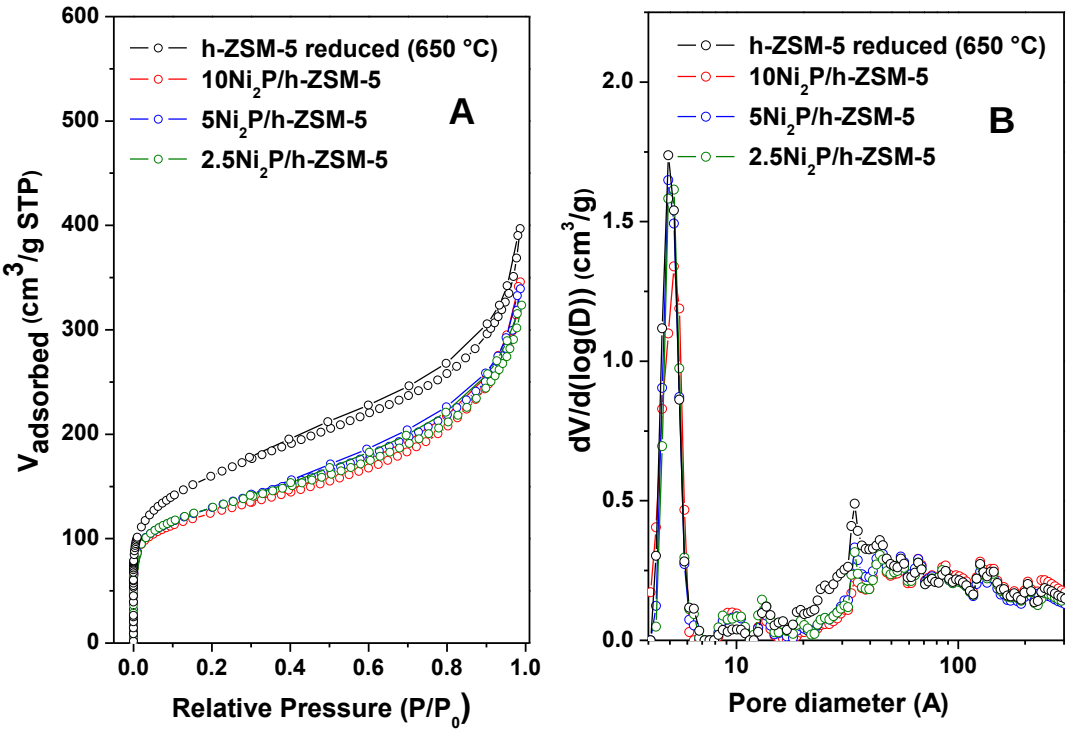

Fig. 3. (A) Ar adsorption-desorption isotherms at 87 K, and (B) pore size distribution estimated from NL-DFT model of Ni_2P/h-ZSM-5 and parent support.

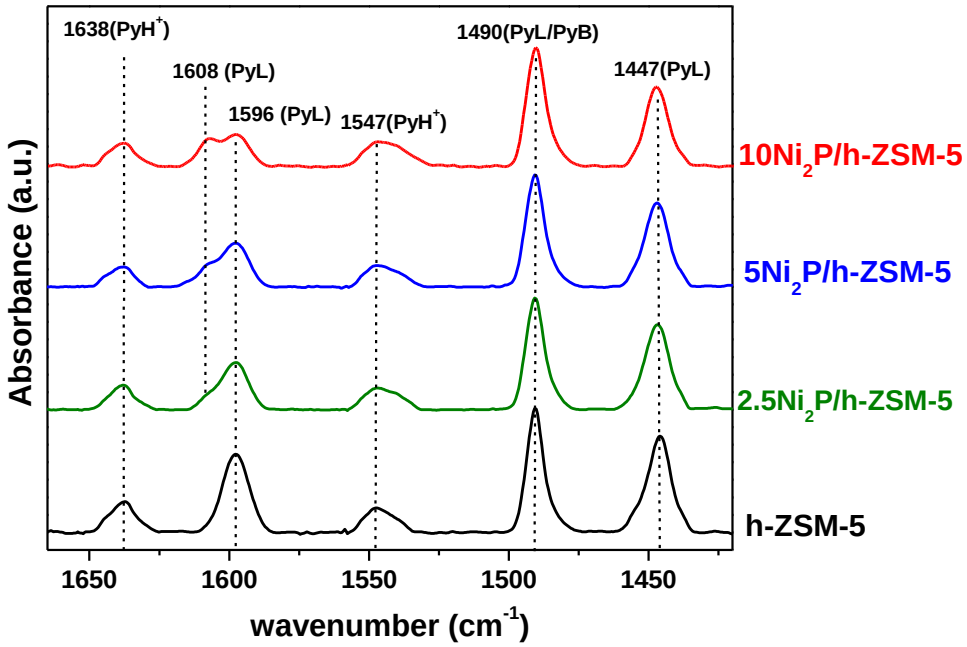

Fig. 4. DRIFT spectra of chemisorbed pyridine over Ni_2P/h-ZSM-5 and parent support.

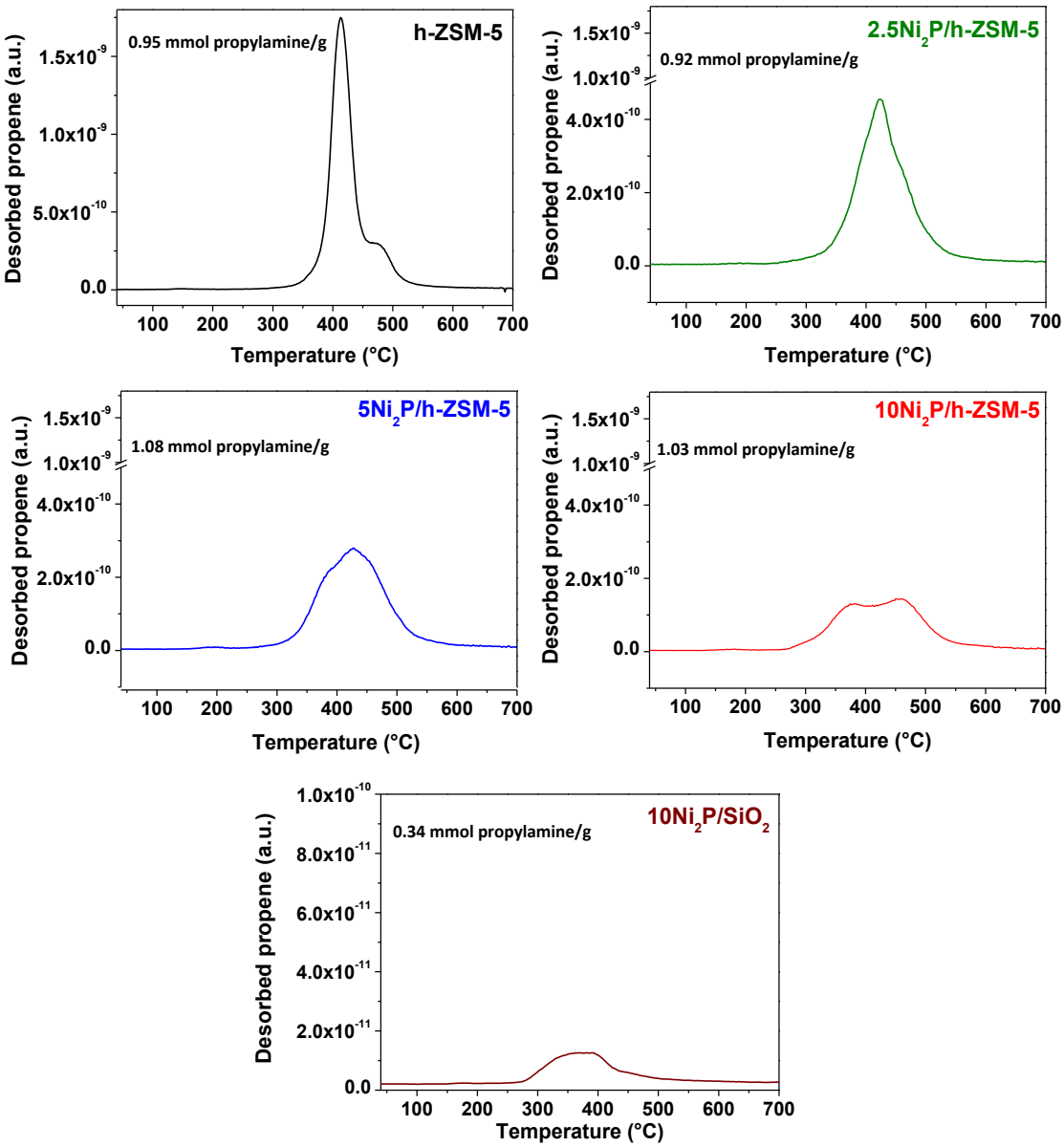

Fig 5. Temperature programmed desorption of reactively formed propene from propylamine decomposition over Ni_2P/h-ZSM-5 and Ni_2P/SiO_2 reference.

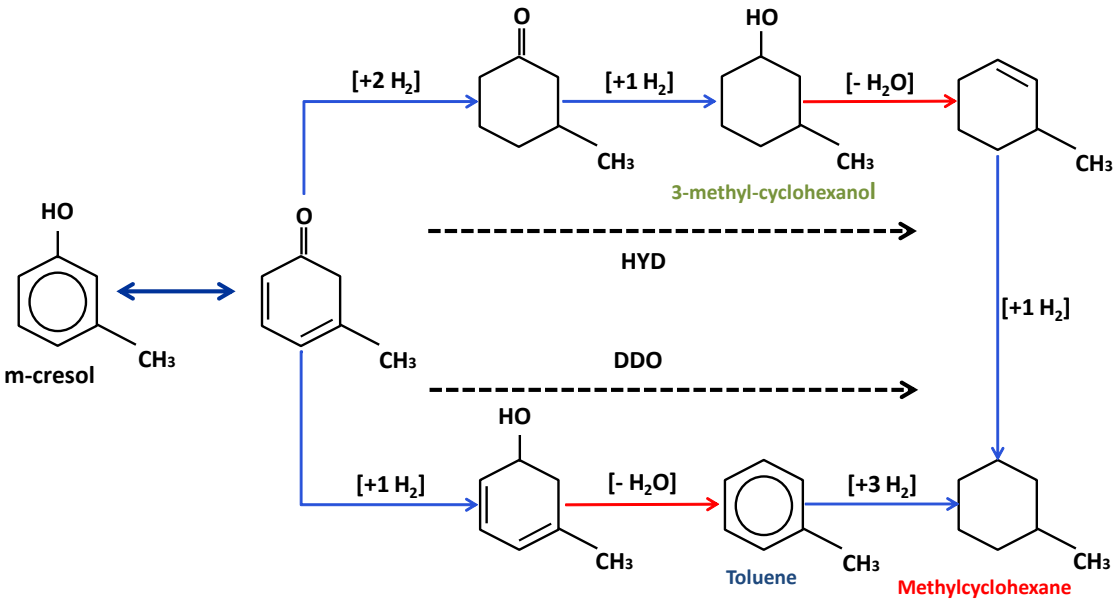

Fig. 6. Proposed reaction pathways in m-cresol hydrodeoxygenation.

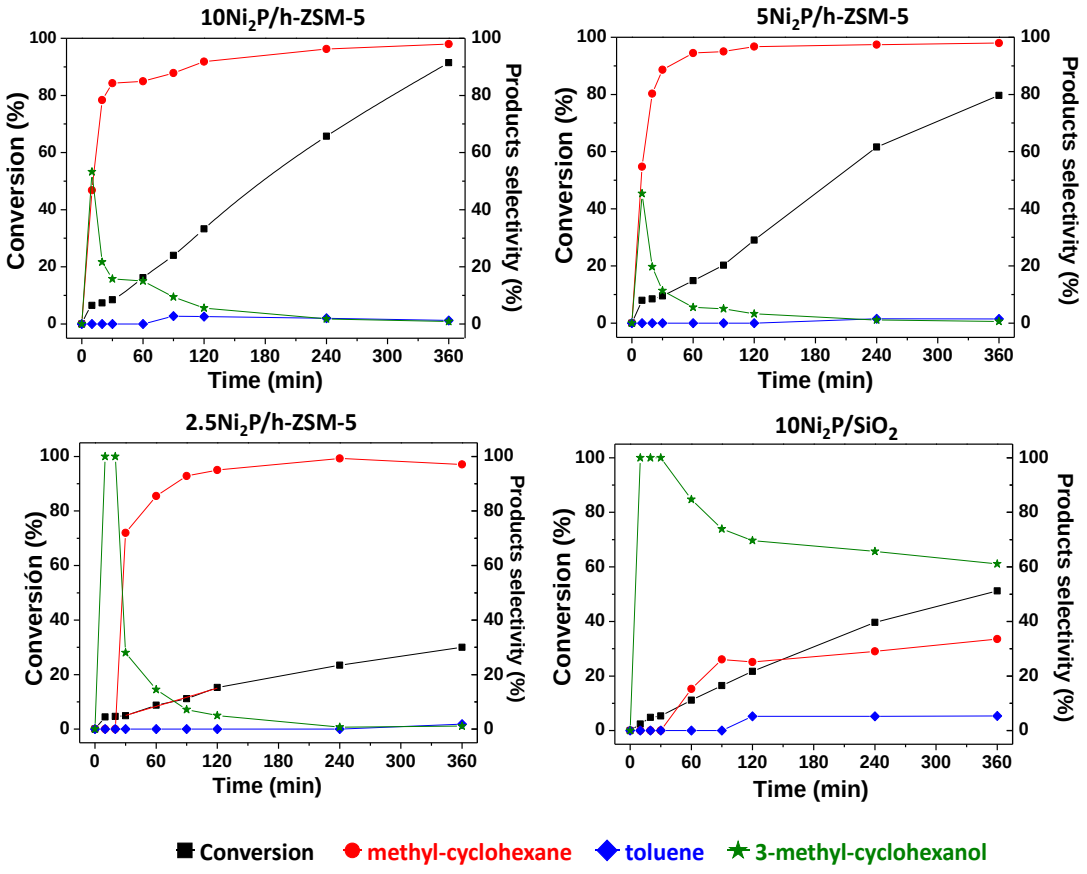

Fig. 7. m-Cresol conversion and product distribution as a function of reaction time over Ni_2P/h-ZSM-5 and Ni_2P/SiO_2 catalysts.

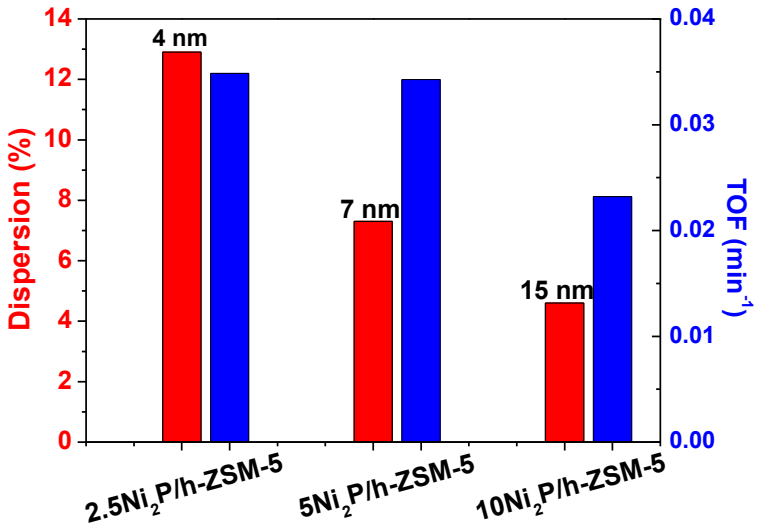

Fig. 8. Correlation between turnover frequency for m-cresol HDO and active phase dispersion of Ni_2P/h-ZSM-5 catalysts.

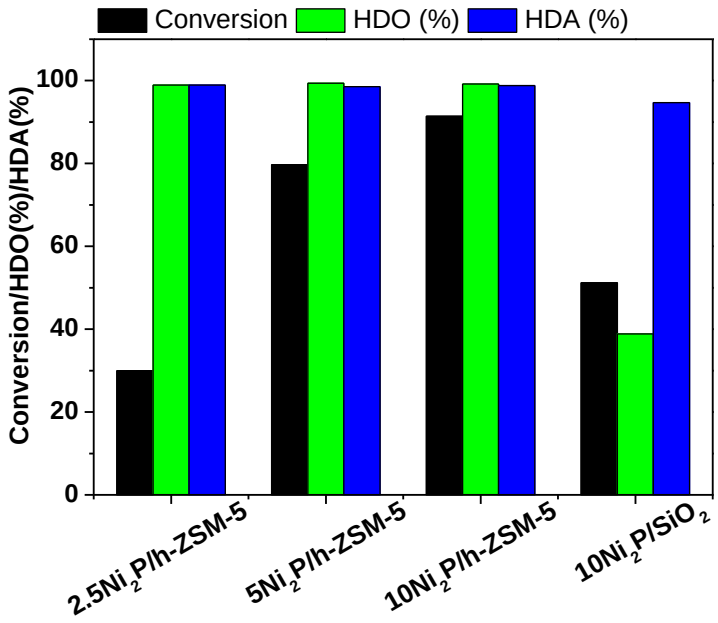

Fig. 9. m-Cresol conversion and hydrodeoxygenation (HDO) and hydrodearomatization (HDA) efficiencies over Ni_2P/h-ZSM-5 and Ni_2P/SiO_2 catalysts.

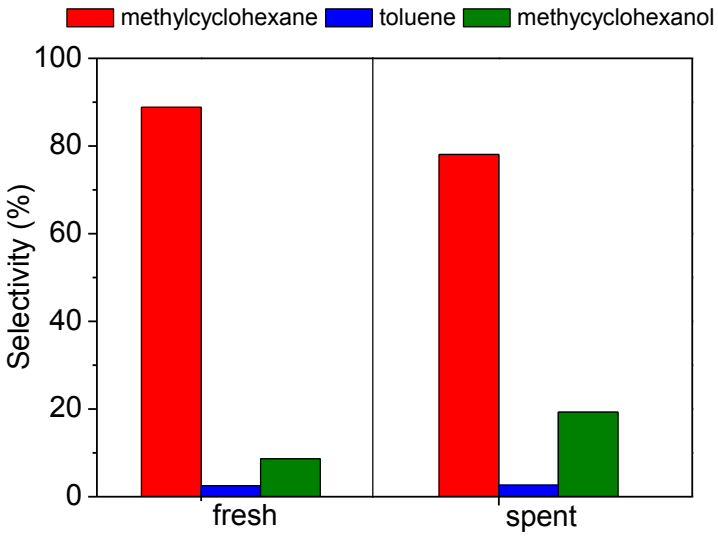

Fig. 10. Reutilization of $5Ni_2P$/h-ZSM-5 catalyst: Products distribution.